Conversion of a piston–cylinder dimensional dataset to the effective area of a mechanical pressure generator

Patrick F. Egan[a] and Eric Stanfield, John Stoup, Christopher Meyer
National Institute of Standards and Technology, 100 Bureau Dr, Gaithersburg, MD 20899

(Received 28 November 2022; Accepted 15 February 2023; Published 20 December 2023)

Recent developments in diameter metrology at NIST have improved the dimensional characterization of piston–cylinder assemblies (PCAs) to unprecedented precision. For the newest generation of PCA, the standard uncertainty on measurement of outer diameter is 12 nm, while uncertainty on measurement of inner diameter is 14 nm. With a high-accuracy dimensional dataset in hand, the task of determining the pressure generated by a specific PCA is reduced to converting diameter (and straightness and roundness) to effective area (and distortion coefficient). Details on how this was done for the artifact PCA2062 are described. PCA2062 was dimensioned in 2017 and 2020; the area repeated within $0.2 \times 10^{-6} \cdot A_0$. The calculation produced estimates of fall-rate and rotation-decay that agree with experimental observations within 12 %. Fall-rate is proportional to the square of gap-width, so the agreement between calculation and measurement validates the dimensional estimate of gap-width within (36 ± 42) nm, where the 42 nm standard uncertainty is governed by the present state of flow theory. The piston-gauge model is buttressed by three comparison tests against a laser barometer, which support a view that PCA2062 is linear and reproducible within 0.2 µPa/Pa. Finally, an estimate of uncertainty in the effective area of a dimensioned artifact is provided: as expected, diameter measurement is the main culprit, but there are open questions with the flow model that preclude an accurate evaluation of the distortion coefficient. For the 530 kPa operating range of PCA2062, distortion is not a significant problem, but the effect would be dominant in assemblies operating 1 MPa and above.

I. INTRODUCTION AND MOTIVATION

An experimental effort is underway to measure the refractivity of helium gas at the level of $10^{-6} \cdot (n-1)$. The motivation is that a precision measurement of helium refractivity at known temperature allows a realization of the pascal, in what is sometimes called the optical pressure scale[1]. One attraction[2] of the optical pressure scale is that it neither relies on artifacts nor restricted materials. Indeed, one stimulant to perfecting the optical realization is that it has potential to settle the twenty-five-year old, unresolved disagreements in mechanical pressure scales—unresolved disagreements which have been at the level of $5 \times 10^{-6} \cdot p$ for piston-gauges[3], and $15 \times 10^{-6} \cdot p$ for mercury manometers[4]. To meaningfully conclude on past disagreements requires that one can compare a new optical realization to a traditional mechanical realization at the highest levels of accuracy. This necessity for a best-effort realization of the mechanical pressure scale motivates the present work. At the National Metrology Institute (NMI) level, the outlook[1,2,5] is that the optical pressure scale will supersede the mechanical scale in terms of accuracy, reliability, and universality.

Towards this best-effort realization of the mechanical pressure scale, three sets of piston–cylinder assemblies (PCA) have been dimensioned, and their effective areas established traceable to the SI meter. These state-of-the-art PCA comprise a 50 mm-diameter fixed piston with a floating and rotating cylinder. The three sets were manufactured in 2014 and coarse dimensioned in 2015. The set PCA2062 was fully dimensionally-characterized in

[a]Electronic mail: egan@nist.gov

2017. In 2020, all three sets PCA2062, PCA2065 and PCA2066 were fully dimensionally-characterized[6]. The set PCA2062 is the exemplar with the best form, and its area and performance are the main focus of this work; PCA2066 plays a role toward the end of the article. While the preceding remarks have framed this piston-gauge development as tandem to the optical realization, it would be remiss not to highlight the present article is alone momentous. It marks the first time a highly-accurate mechanical pressure scale has been established for the nation and based on NIST dimensions. The achievement reifies a generation of dedicated effort in dimensional metrology, with a steadfast and methodical drive toward improved capability.

Next follows some details on how the dimensional datasets were converted to effective area, which rely heavily on two references by Sabuga and coworkers[7,8]. The procedure begins by fusing together three separate dimensional inputs (diameter, straightness, and roundness) to form a birdcage model of the artifact. Then, the pressure-induced distortion is added to the birdcage; the distortion is calculated by finite-element methods, and uses one parameterized input, which is the pressure distributed down the gap between the piston and cylinder. This distributed pressure is calculated by the theory of rarefied gas dynamics. Finally, the cross-sectional area of the distorted birdcage is calculated. To explain the calculation, Section II will logically work backwards: starting from the output (pressure equals force divided by area), and unwinding step-by-step to the input (dimensions). A block diagram of the calculation procedure is shown in Fig. 1(a), and the explanation will move from bottom to top. After the calculation, a lengthy discussion follows in Section III, which describes the uncertainty of a generated pressure, together with some customary diagnostics. Finally, the article concludes with Section IV, which features some additional tests on piston-gauge performance via comparison to a highly precise laser barometer.

II. CALCULATION PROCEDURE

The mechanical pressure generated by the piston-gauge is given by

$$p_{\mathrm{mpg}} = \frac{mg}{A_0\left[1+(t_{90}-20)2\alpha_{\mathrm{WC}}\right](1+b\Delta p)} + p_{\mathrm{vac}}, \tag{1}$$

where m is a mass load and g is local gravity. The effective area $A_{\mathrm{eff}} = A_0(1 + b\Delta p)$ is described more below, and is estimated chiefly by dimensional measurements made at $t_{90} = 20$ °C; when the piston-gauge operates away from this reference temperature, its diameter (effective area) should be scaled for the thermal expansion α_{WC}. (The notation t_{90} refers to temperature measurement on the international temperature scale of 1990.) As pressure inside the cylinder increases, the piston and cylinder deform, thus changing the diameter (effective area); the deformation parameter b accounts for pressure-induced distortion. Finally, Eq. (1) should balance for pressure acting outside the cylinder; in the present case, operation is in "absolute mode" and the pressure outside the cylinder is pumped to $p_{\mathrm{vac}} < 0.3$ Pa, and measured with a capacitance diaphragm gauge.

The effective area A_{eff} of the PCA should consider forces caused by flow and friction in the gap—the space between the piston and cylinder, which is approximately 580 nm. Historically, these forces were estimated by the theory of Dadson[9], which assumed viscous flow. The more recent theory of Sharipov[7,10] is based on rarefied gas dynamics, which computes a flow coefficient determined by the level of rarefaction for all pressures and dimensions distributed down the gap. For a pressure differential across the gap $p_1 - p_2$ (in this case $p_2 = p_{\mathrm{vac}}$), Sabuga, Sharipov, and Priruenrom[7] write the area $A_0 = A_1 - A_2 - A_3$

having three components[11]

$$\begin{aligned} A_1 =& \frac{\pi \mathcal{G}_{\mathrm{c1}}^2 p_1 - \pi \mathcal{G}_{\mathrm{c2}}^2 p_2}{p_1 - p_2} \\ A_2 =& \frac{\pi \int_0^{l_\mathrm{c}} h_z \mathcal{G}_\mathrm{c} \frac{\mathrm{d}p_z}{\mathrm{d}z} \mathrm{d}z}{p_1 - p_2} \\ A_3 =& \frac{2\pi \int_0^{l_\mathrm{c}} p_z \mathcal{G}_\mathrm{c} \frac{\mathrm{d}\mathcal{G}_\mathrm{c}}{\mathrm{d}z} \mathrm{d}z}{p_1 - p_2}. \end{aligned} \tag{2}$$

The effective area A_eff is found by calculating A_0 for several different p_1, and extrapolating $(p_1 - p_2) \to 0$; the distortion coefficient b is deduced from the slope of the extrapolation. In A_0, the first component A_1 is the area upon which the mass-force acts, and depends on the radius (generatrix) at top $\mathcal{G}_{\mathrm{c1}}$ and bottom $\mathcal{G}_{\mathrm{c2}}$ of the cylinder. The generatrix of a cylinder, described below, is obtained as the line that minimizes deviations between three sets of dimensional measurements: straightness, roundness, and point-to-point diameter. The other two components in Eq. (2) are A_2 and A_3, and arise from the drag forces owing to gas flow in the gap and surface curvature; both of these components require knowledge of the pressure distribution p_z along the gap, and drive the gap dimensions to be updated for pressure-induced distortion. The width of the gap $h_z = \mathcal{G}_\mathrm{c} - \mathcal{G}_\mathrm{p}$ is the difference between the generatrixes of cylinder and piston. The height of the cylinder $l_\mathrm{c} = 40$ mm includes a 2 mm extrapolation of diameter measurements at both ends of the cylinder. The coordinate system is shown in Figure 2(a); z is along the cylinder axis and x is radial; the variables $\mathcal{G}_\mathrm{c,p}$, h_z, and p_z are all functions of z.

The calculation is iterative[12]: First there is a calculation of the pressure distribution from p_1 down to p_2 along the gap

$$p_z = p_1 + (p_2 - p_1) \frac{\int_0^z \left[h_z^2 G_\mathrm{P}\right]^{-1} \mathrm{d}z}{\int_0^{l_\mathrm{c}} \left[h_z^2 G_\mathrm{P}\right]^{-1} \mathrm{d}z}, \tag{3}$$

which requires the Poiseuille coefficient[10,13]

$$G_\mathrm{P} = a_{00} + \begin{cases} \frac{1}{2\sqrt{\pi}} \ln \frac{\mathcal{G}_\mathrm{c}}{h} + \frac{\pi}{2} & \text{for } \delta \le 5 \times 10^{-4} \\ \sum_i a_i \log(\delta)^i & \text{for } \delta > 5 \times 10^{-4}, \end{cases} \tag{4}$$

the interpolation of which is based on evaluation of the rarefaction parameter[10,13]

$$\delta_z = \frac{p_z h_z}{\eta v_\mathrm{mp}}, \tag{5}$$

where η is gas viscosity, and $v_\mathrm{mp} = (2RT/M)^{1/2}$ is the most probable speed and depends on the gas constant R, temperature T, and molar mass M. For G_P at $\delta > 5 \times 10^{-4}$, a 12th-order polynomial is fit to the solution[10] of the one-dimensional, infinite plate, planar Poiseuille flow, with coefficients a_i

$$\begin{array}{lll} a_0 = 1.547801 & a_1 = -1.661399 \times 10^{-2} & a_2 = 6.736396 \times 10^{-1} \\ a_3 = 2.475631 \times 10^{-1} & a_4 = 1.034375 \times 10^{-1} & a_5 = 1.105164 \times 10^{-1} \\ a_6 = 8.492110 \times 10^{-2} & a_7 = 2.283521 \times 10^{-2} & a_8 = -5.879727 \times 10^{-3} \\ a_9 = -5.427568 \times 10^{-3} & a_{10} = -1.438483 \times 10^{-3} & a_{11} = -1.742273 \times 10^{-4} \\ a_{12} = -8.217794 \times 10^{-6}. & & \end{array}$$

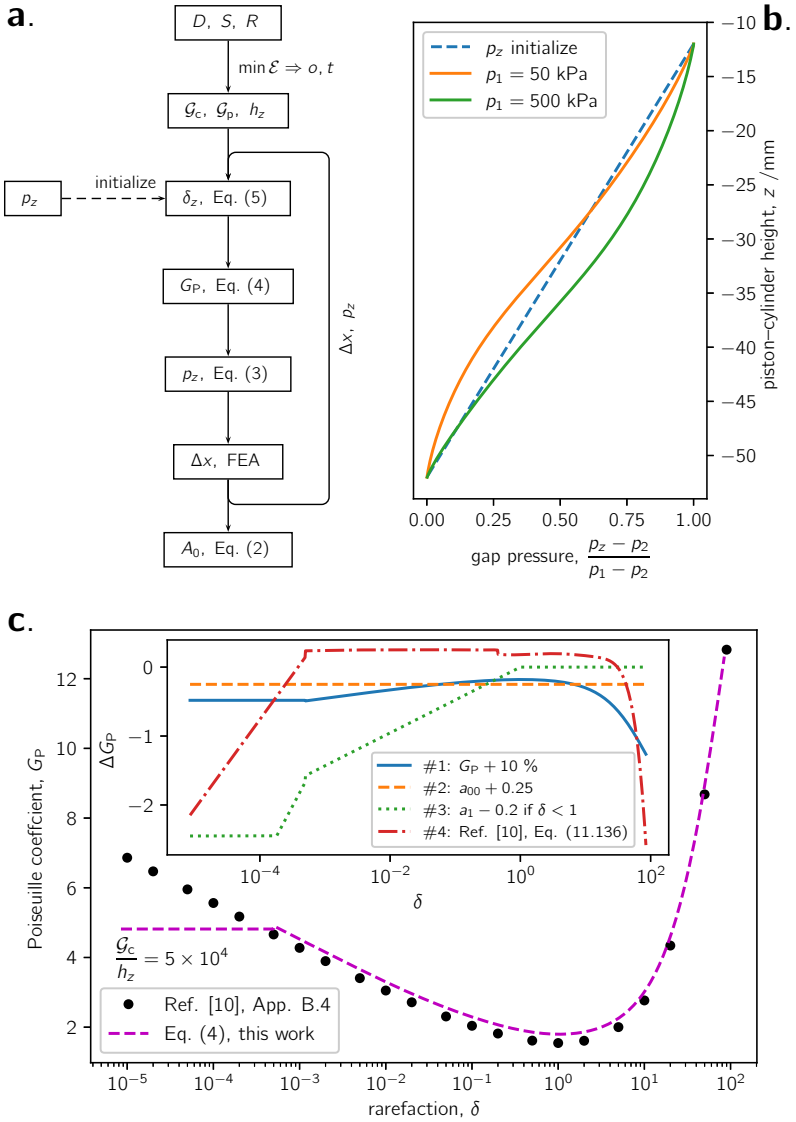

FIG. 1. (a.) Block diagram of the procedure to calculate A_0. (b.) Pressure distribution down the gap p_z for two cases in helium, $p_1 = 50$ kPa and $p_1 = 500$ kPa, and with $p_2 = 0$. (c.) Poiseuille flow coefficient from Sharipov[10] and modified to the physical situation of the present work. The inset figure shows the difference between Eq. (4) and four error cases covering $u(G_P)$.

A numerical algorithm to calculate G_P is given in Ref. 10. The function of Eq. (4) is plotted in Figure 1(c), together with output from the algorithm of Ref. 10; the function Eq. (4) is modified from Ref. 10 as follows: the two-part function of Eq. (4) is clipped[7] as $\delta < 4 \times 10^{-4}$ to approximate the annular flow[14] in the limit $\frac{\mathcal{G}_P}{\mathcal{G}_c} \to 1$. This patch addresses the problem with the infinite plate solution, in which G_P becomes infinite as $\delta \to 0$. The clipping threshold is specific to each PCA geometry[7] by the quotient $\frac{\mathcal{G}_c}{h_z}$; for PCA2062, even at helium pressures as low as $p_1 = 10$ kPa (and $p_2 = 0$), the annular flow approximation applies to less than 2 % of the gap region, and its influence on A_0 is negligible. The function Eq. (4) allows for a tangential momentum accommodation coefficient of 0.9, by setting the offset factor $a_{00} = 0.25$. Lack of knowledge about the accommodation coefficient is a main contributor to uncertainty in the theory of rarefied gas dynamics; the four perturbations to

G_P, plotted in the inset of Figure 1(c), are relevant to the uncertainty analysis, discussed in Section III.

In the calculation of p_z, the terms p_z and δ_z are interdependent, and so iteration is required for convergence. (To startup, δ_z is initialized with a linear distribution of pressure down the gap.) The procedure should also be iterated for h_z, because the width of the gap changes, caused by pressure-induced distortion of the piston and cylinder. The pressure-induced distortion is computed using finite-element analysis (FEA), which is parameterized for the pressure load p_z applied to the gap, obtained by calculation of Eq. (3). This all works with a master script which handles several things: (i) calculates p_z based on the most recent estimate of G_P and h_z; (ii) dynamically updates two FEA scripts (one piston script and one cylinder) with p_z and runs the FEA program; (iii) extracts/imports Δx along the PCA engagement region from the FEA displacement results; (iv) updates $\mathcal{G}_\mathrm{p}$ and $\mathcal{G}_\mathrm{c}$ for the respective Δx, recomputing p_z and G_P; and (v) iterates. An overview block diagram of the calculation procedure is shown in Figure 1(a). The computed area converges within $10^{-8} \cdot A_0$ after two iterations [see Figure 3(a)], and the main advantage of this "closed-loop" implementation is that numerical investigation of model sensitivity to input errors can be performed with versatility. Another closed-loop benefit is demonstrated in Figure 3(c): the effective area and distortion coefficient can be calculated throughout the cylinder fall down the piston—something impractical to do with an open-loop implementation which hand-transcribes settings from one program to another. The FEA is shown in Figure 2(a), which is actually two separate simulations of piston and cylinder, which have been clipped to the same Δx colorscale and combined (the width of the gap is arbitrarily exaggerated in x). The FEA model is axisymmetric about $x = 0$, and the boundary conditions are also annotated in Figure 2(a): ① pressure p_1 applied to partial inner surface of cylinder, ② pressure p_1 applied to inner, top, partial outer, and partial bottom surface of piston, ③ distributed (gap) pressure p_z applied to engaged segments of piston and cylinder as a function of z, ④ piston constrained in z (by clamped o-ring), ⑤ lip of cylinder constrained in z (by mass load). The distorted profiles of the piston outer diameter and cylinder inner diameter, along the region of engagement, are extracted from the FEA and added to the generatrix (actual dimensional measurements) in Figure 2(b), with $p_1 = 500$ kPa. Figure 2(b) is also annotated with the locations of the pressure "regions" p_1, p_z, and p_2.

The dimensional inputs to Eq. (2) are the generatrixes of piston and cylinder. Dimensional characterization provided high-density data traces of roundness and straightness, and low-density data on point-to-point diameter. The best estimate of the artifact geometry is obtained by fusing together (synchronizing[8]) the intersecting points in the three sets of measurements. Sabuga and Priruenrom[8] found the generatrix and directrix

$$\begin{aligned} \mathcal{G}(z) &= S_\theta(z) + o + tz \\ \mathcal{D}(\theta) &= R_z(\theta) + q + w\cos\theta + v\sin\theta \end{aligned} \tag{6}$$

by adjusting the measured straightness $S_\theta(z)$ and roundness $R_z(\theta)$ by the model parameters o, t, q, w, v. Straightness $S_\theta(z)$ is a function of height z, and is indexed for each trace made in azimuth θ; the parameters offset o and taper t are vectors of dimension equal to the number of traces in θ (which is eight for both piston and cylinder). Roundness $R_z(\theta)$ is a function of θ, and is indexed for each trace made in z; the parameters q, w, and v are vectors of dimension equal to the number of traces in z (which is eight for the piston and five for the cylinder). The model parameters are deduced by least-squares minimization of the objective function

$$\mathcal{E}^2 = \min_{o,t,q,w,v} \sum_{i=1}^{5} \left(\frac{\sum e_i^2}{N_i} \right), \tag{7}$$

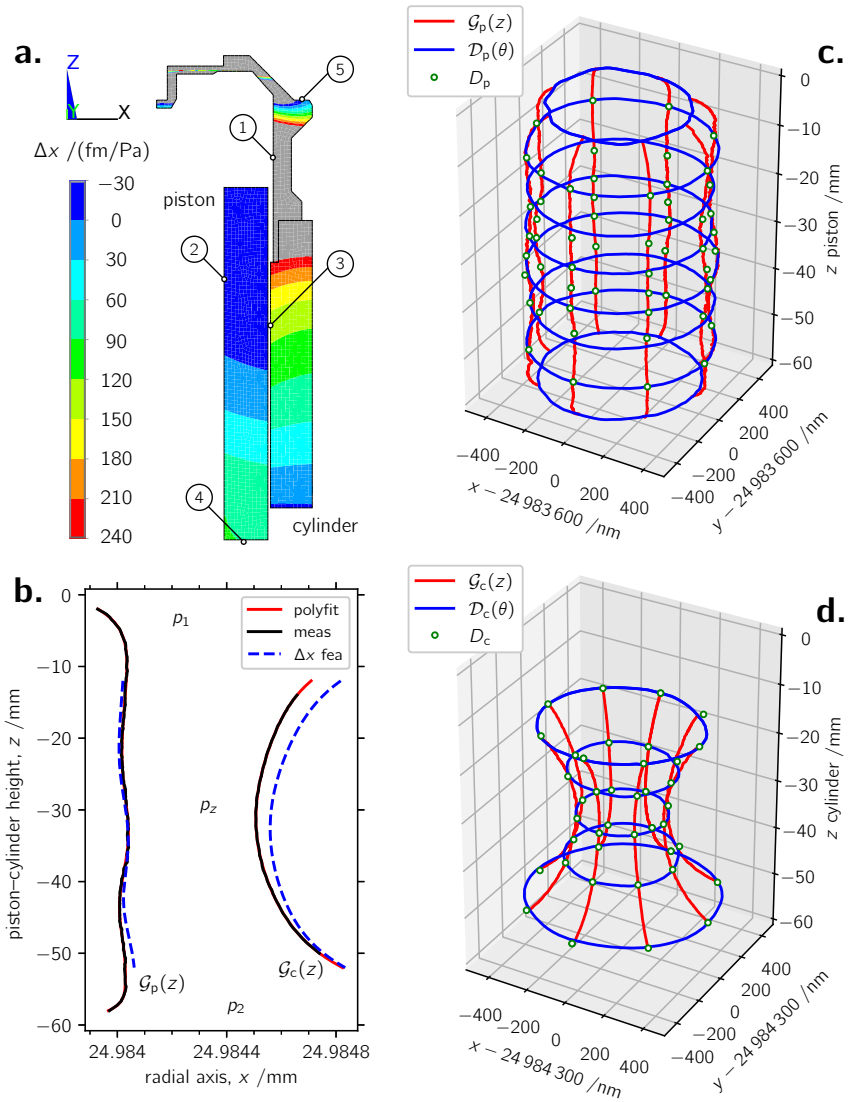

FIG. 2. (a.) Finite-element model of pressure-induced distortion in the piston and cylinder. (b.) Least-squares-adjusted generatrixes of piston and cylinder, with overlay of pressure-induced distortion at $p_1 = 500$ kPa and $p_2 = 0$. (c. and d.) "Birdcage" model of piston and cylinder constructed by fusing three sets of dimensional data: straightness, roundness, and point-to-point diameter.

which has

$$\begin{aligned} e_1 &= \mathcal{G} - \mathcal{D} \\ e_2 &= \frac{D - (\mathcal{G} + \mathcal{G}')}{2} \\ e_3 &= \frac{D - (\mathcal{D} + \mathcal{D}')}{2} \\ e_4 &= \frac{D_{\text{ref}}}{2} - \mathcal{G}_{\text{ref}} \\ e_5 &= \frac{D_{\text{ref}}}{2} - \mathcal{D}_{\text{ref}}, \end{aligned} \tag{8}$$

and D are the measured point-to-point diameters. (The term $\mathcal{E}$ is the root-mean-square

error of the optimization, and is a metric of statistical uncertainty. The integer N_i is the sample size of each residual error matrix e_i.) The flow calculation of Sabuga, Sharipov, and Priruenrom[7] uses the generatrix $\mathcal{G}$ of the piston and cylinder to calculate the cross-sectional area that best describes a three-dimensional artifact. The residual matrices e_4 and e_5 in Eq. (8) are setup as reference points to define the coordinate system in which the dimensional adjustment is performed. This means they are setup as sparse matrices of four diameters; two at different z heights and two at different θ azimuthal angles; the choice of height and angle is arbitrary. The notation $\mathcal{G}'$ and $\mathcal{D}'$ refers to the generatrix and directrix at the opposite azimuthal orientation.

The least-squares adjusted datasets are shown in Figure 2(c) and (d); these plots are sometimes called the "birdcage"[15,16]. The plot of the piston in Figure 2(c) has been scaled in the radial axis by subtracting 49.9672 mm from the diameter; the plot of the cylinder in Figure 2(d) has had 49.9686 mm subtracted from the diameter. Once the vectors o and t have been found by the least-squares adjustment of the intersecting points, each straightness trace can be converted to its respective $\mathcal{G}$. The result is a set of eight $\mathcal{G}$ which are a function of z, and are indexed for each straightness trace in θ. For calculation of A_0, the eight $\mathcal{G}$ are averaged over θ.

Finally, this dimensional characterization of $\mathcal{G}$ is used in the area calculation of Eq. (2), to produce a determination of $A_0 = A_1 - A_2 - A_3$ as a function of pressure. The A_0 result is plotted in Figure 3(b); the relative contributions of A_2 and A_3 are shown in the inset of Figure 3(b). From this, the effective area of PCA2062 has been determined as

$$A_{\text{eff}}^{2062} = 1961.0292(37)\left[1 + 5.12(73) \times 10^{-12}\frac{\Delta p}{\text{Pa}}\right]\ \text{mm}^2$$

in helium at 20 °C and absolute mode, and valid for the dimensional characterization of 2020. The distortion coefficient b is best described by a linear term. The estimation of b from the slope of the line in Figure 3(b) is for a monolithic assembly. The final estimate given above is 2.6 % smaller than the slope of the line in Figure 3(b); this reduction in distortion is based on a finite-element simulation of a 0.1 mm epoxy joint between the titanium (cap) and tungsten carbide that forms the hollow cylinder assembly. What follows next is the uncertainty budget for this determination.

III. UNCERTAINTY EVALUATION

The uncertainty budget for the pressure generated by a piston-gauge is given in Table I. Most entries concern the proportional term, but there are two entries which are best split into an offset term. With this splitting of terms, combined uncertainty is slightly overestimated in parts of the pressure range. But the general message is that uncertainty is dominated by the proportional term throughout most the working range. It is only below 50 kPa that the offset term becomes significant (which is the lower tenth of the working range).

The budget in Table I evaluates each input parameter to Eq. (1), and the entries in the table are discussed below. Some of these assessments may be considered controversial, owing to their relative largeness compared to antecedent estimates of piston-gauge uncertainty; here, the intention is to be conservative rather than controversial. Throughout this article, the notation $u(x)$ is used to denote the standard uncertainty of the quantity x. Unless otherwise stated, all uncertainties in this work are one standard uncertainty, corresponding to approximately a 68 % confidence level.

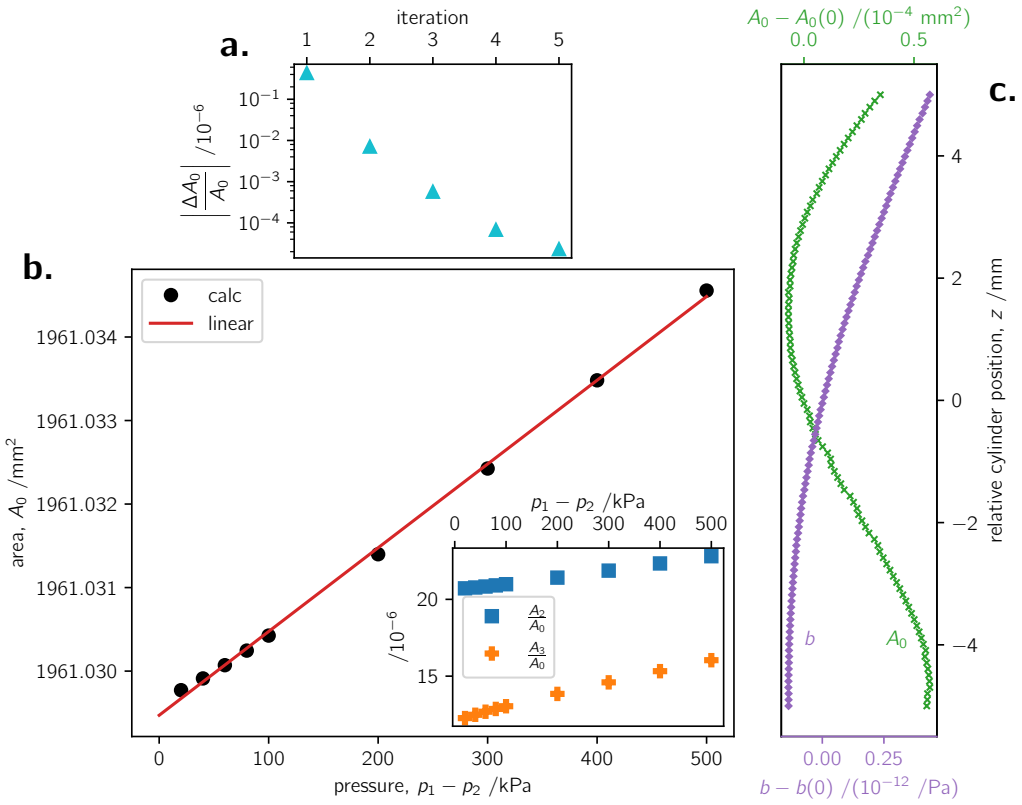

FIG. 3. (a.) Convergence of the p_z and FEA iteration loop. (b.) Calculated area as a function of pressure for the piston–cylinder assembly PCA2062 in "absolute mode" with $p_2 = 0$. Inset: relative contributions of A_2 and A_3 to A_0. (c.) Change in A_0 and b, relative to values at $z = 0$, as the cylinder falls down the piston.

A. The Main Contributor, $u(A_0)$

1. Dimensional Uncertainty

Diameter measurement was a massive effort, and required the improvement of an old instrument (sphere diameter in a Fizeau-type interferometer)[17], the establishment of a new instrument (cylinder and sphere diameter in a laser micrometer)[18], and two forty-year-old coordinate-measuring machines (CMM) in shipshape condition. The breadth and scope of the development is described by Stoup *et al.*[6], and here only a brief synopsis is provided. The outer diameter of the piston was measured with an ultrahigh accuracy laser micrometer. The inner diameter of the cylinder was measured with the CMM in comparison mode: the CMM effectively operated as a null-comparator, comparing the (unknown) diameter of the cylinder relative to the (known) diameter of the piston. The probe of the CMM was mastered with precision spheres, whose diameters were independently determined with the Fizeau-type interferometer. These master spheres also provided a crosscheck between the Fizeau-type interferometer and the laser micrometer. Additional reference artifacts and crosschecks were strategically employed in the characterization to achieve state-of-the-art performance in a CMM-as-comparator: Ref. 6 has the details. One strength of this diameter measurement is redundancy, with different artifacts being cross-validated across multiple measuring machines, and each machine having its unique and understood systematic errors. The uncertainty[6] for the piston diameter (outer) was 12 nm, and the uncertainty for the cylinder diameter (inner) was 14 nm. The entry D in Table I treats the two diameters

as fully correlated, and the net uncertainty in the effective diameter of the assembly is $[u(D_\mathrm{p}) + u(D_\mathrm{c})]/2$.

In addition to the measurement uncertainty in diameter, there is uncertainty on how well the three dimensional datasets can be fused together[6]. The least-squares adjustment described by Eq. (6) and Eq. (7) builds a generatrix and directrix to form a model birdcage—a wireframe whose coordinates depend on the intersecting points of diameter, straightness, and roundness. Residual deviation persists between the three datasets, because each measuring machine has its own error, and there are likely small changes in orientation/indexing as the artifacts are moved between machines and measured. This residual deviation means that there is statistical uncertainty in the generatrix $\mathcal{G}$. The estimate of this statistical uncertainty is the entry $\mathcal{E}$ in Table I. The term $\mathcal{E}$, defined in Eq. (8), is the root-mean-square error of the objective function after minimization, and reflects net deviation between the three error matrixes, $\mathcal{G} - \mathcal{D}$, $D/2 - \mathcal{G}$, and $D/2 - \mathcal{D}$. The result for the piston $\mathcal{E}_\mathrm{p} = 4.8$ nm, and for the cylinder $\mathcal{E}_\mathrm{c} = 8.5$ nm; these computed results are in terms of radius. Attempts were made[6] to estimate residual strain in the birdcage, and assess the flexibility available to $\mathcal{G}$ due to lack of coverage in the D, S, R-dataset. This was done by Monte Carlo simulation. The idea was to deliberately remove dimensional data from the birdcage, and simulate the resulting effect on $\mathcal{G}$. The conclusion from simulation was that $\mathcal{E}$ adequately covers all expected variation in $\mathcal{G}$, for birdcage sampling as dense as Figure 2(c) or (d). The entry $\mathcal{E} = (\mathcal{E}_\mathrm{p}^2 + \mathcal{E}_\mathrm{c}^2)^{1/2}$ in Table I treats the imperfect form of piston and cylinder as uncorrelated in their contribution to uncertainty in the effective diameter of the assembly. Finally, the component $\mathcal{E}$ only covers uncertainty in fusing together three dimensional datasets; a related component—the effect of imperfect cylindricity on flow—is a separate entry, discussed below.

Mechanical probing can only approach the actual "edge" defining the end of the piston and cylinder, because of the finite probe size and instability in fixturing. Therefore, extrapolation is used to estimate the cylinder diameter. As can be seen in Figure 2(b), the measured cylinder radius is increasing by approximately 25 µm/m at the extremity; therefore, $\mathcal{G}_\mathrm{c}$ should be extrapolated across 2 mm to determine diameter at the point of engagement. Because the cylinder of PCA2062 has a uniquely smooth and predictable curvature, one can have confidence in this extrapolation within 10 %. This uncertainty component is labeled "extrapolation" in Table I. This extrapolation of the diameter measurements to the cylinder end increases the effective area by $3.5 \times 10^{-7} \cdot A_0$.

Deviations from the 20 °C reference temperature at which the piston and cylinder are dimensioned should be compensated for thermal expansion of the artifacts. For typical use, the piston-gauge PCA2062 operates in a lab stabilized to (20 ± 0.1) °C, and the small corrections for thermal expansion require moderately accurate thermometry of the PCA. The temperature of the PCA was measured with onboard resistance thermometers; these resistance thermometers were calibrated near 20 °C by direct comparison to a calibrated thermistor, all placed in an isothermal block. The uncertainty in this calibration procedure is within a few millikelvin, and despite operating in a lab with very small thermal fluctuations/gradients, a 20 mK uncertainty is assigned to the temperature of the PCA. The relatively large assessment is because the resistance thermometer is inside the post of the piston-gauge, and does not directly measure the temperature of the PCA; the 20 mK covers gradients that potentially develop between the thermometers and PCA. For the thermal expansion coefficient of tungsten carbide, the nominal value $\alpha_\mathrm{WC} = 4.6 \times 10^{-6}$ /K is used. For the 20 mK uncertainty in PCA temperature, the 50 mm diameters can therefore be confidently compensated for temperature within 4.6 nm. This component is labeled α_WC in Table I. Because the nominal value α_WC is used, this temperature-dependent diameter uncertainty is only valid for operation near 20 °C.

A component "compression" is added to the budget, which accounts for uncertainty in the piston diameter, because it is clamped between two o-rings. Though the effect is small—change in diameter $\Delta D \approx \frac{4\mu F}{\pi D E}$, given by Poisson's coefficient μ and Young's modulus E—it is difficult to have confidence in the compression force F of the clamped o-ring, and possible "barreling" caused by friction. Manufacturer handbooks give rules-of-thumb, based on o-

TABLE I. Relative standard uncertainty in mechanical pressure generated by a dimensioned piston-gauge has been split into an offset and proportional term.

component	$u(p_{\mathrm{mpg}}) \times 10^6$
A_0	
dimensional	1.7
D, 13 nm	
$\mathcal{E}$, 19.8 nm	
extrapolation, 10 nm	
α_{WC}, 4.6 nm	
compression, 3 nm	
instability, 17.8 nm	
flow	0.7
RGD, 2.9×10^{-4} mm^2	
$\mathcal{G}$, 13×10^{-4} mm^2	
h_z, 0.1×10^{-4} mm^2	
b	0.4
m	54 mPa + 0.1
g	0.2
p_{vac}	2.5 mPa
combined ($k = 1$)	$\left[(54\ \mathrm{mPa})^2 + (1.9\ \mu\mathrm{Pa/Pa})^2\right]^{1/2}$

ring durometer, diameter, and compression, suggesting a clamping force of approximately 2.6 N/mm of lineal o-ring. The rule-of-thumb is assumed reliable within a factor of 2, which yields the 3 nm uncertainty in the diameter caused by o-ring compression force. [Another "compression" that should be considered is compressibility of the PCA, because the artifacts are dimensioned at atmospheric pressure, but operate in vacuum (absolute mode). Compressibility is accounted for in the FEA of Figure 2(a), and only changes area by $2 \times 10^{-7} \cdot A_0$. Its uncertainty contribution is effectively absorbed into $u(\mathcal{G})$, discussed below.]

The last dimensional component in Table I is instability of the artifacts. The assembly PCA2062 was initially dimensioned in 2017. Its calculated area from the 2017 dimensioning was 0.2 µPa/Pa smaller than the present report. The mean piston diameter was 18.8 nm smaller; the mean cylinder diameter was 16.8 nm larger. At this level, and with only a two-sample history, it is not clear whether the gauge is unstable, or if reproducibility in the measurement procedure is being validated, or if wear is a possible explanation. (Based on almost identical straightness and roundness traces in both dimensional datasets between 2017 and 2020, it is felt that wear is an unlikely explanation.) Nevertheless, at this early stage of the gauge's control chart, a 17.8 nm uncertainty is assigned to temporal stability of the artifact's dimensions. Additional dimensional checks over the next decade may reduce this uncertainty component.

2. Flow Uncertainty

No clear uncertainty budget has been developed for the rarefied gas dynamics model of Sharipov. Lacking this knowledge, a first statement is that, for the present geometry, the classical Dadson theory predicts A_0 to be 2×10^{-7} smaller than Sharipov. (As Sutton and Fitzgerald[19] have highlighted, viscous flow—Dadson theory—has almost no application to modern piston–cylinder assemblies, with 500 nm gap-widths operating sub-megapascal. Nevertheless, Sutton and Fitzgerald[19] also made arguments that the choice of flow model only influences A_0 at fractions of a part per million. This fact was verified by Sabuga[20]. The present work agrees that A_0 is weakly dependent on the flow model.) Second, reasonable uncertainty estimates for the viscous slip coefficient have negligible effect on G_{P} (and A_0,

TABLE II. Comparison of experimental fall-rate to theory and Eq. (9). PCA2062 in absolute mode, $p_2 < 0.3$ Pa. Numbers in brackets express standard uncertainties. Viscosities used are from REFPROP[27], which at 293.15 K are: $\eta_{\mathrm{He}} = 19.63$ µPa s, $\eta_{\mathrm{Ar}} = 22.31$ µPa s, $\eta_{\mathrm{N_2}} = 17.57$ µPa s.

	v_{fall} /(nm/s)								
	He			Ar			N_2		
p_1 /kPa	exp.	theory	% diff.	exp.	theory	% diff.	exp.	theory	% diff.
43	609(66)	652(75)	−6.6	180(19)	200(24)	−10.2	209(23)	239(28)	−12.6
93	597(64)	639(76)	−6.6	207(22)	221(24)	−6.4	245(26)	267(29)	−8.5
195	651(70)	694(79)	−6.1	273(30)	287(25)	−4.7	330(36)	352(31)	−6.3
297	726(78)	781(82)	−7.0	349(38)	367(33)	−4.9	417(45)	453(40)	−8.0
399	806(87)	887(85)	−9.1	442(48)	458(41)	−3.4	519(56)	569(50)	−8.6
501	908(98)	1009(91)	−10.0	546(59)	559(49)	−2.2	648(70)	695(61)	−6.8

shown by Sharipov *et al.*[21]). Last, an attempt was made to estimate the error bounds on G_{P} based on information provided by Sharipov and Seleznev[22] and Sharipov[10]. The largest uncertainty component in G_{P} is the tangential momentum accommodation coefficient, which describes energy transfer at the gas–surface interface[23]; the coefficient is an experimental input to the scattering kernel that underpins the theoretical calculation[13,24] of G_{P}; the coefficient is unity for perfectly diffuse scattering, and zero for specular reflection. This accommodation coefficient is species- and roughness-dependent, and for polished tungsten carbide is unknown. Surveys[24,25] of measurements for the accommodation coefficient show much variability, and Ref. 25 concludes that a "range of 0.80–1.02 seem to encompass almost all data available in the literature for monatomic gases irrespective of the Knudsen number and surface material." A more recent extraction from highly accurate acoustic resonator experiments in helium and argon also showed some variability[26], and noted that deriving an accommodation coefficient from experimental data is nontrivial. Since no information is available for the accommodation coefficient of polished tungsten carbide, Ref. 25 is used as a guideline, and a value 0.9 ± 0.1 is assumed. Refs. 10, 13, and 22 show that an error of 0.1 in the accommodation coefficient causes, to first-order, a 0.25 offset in G_{P} throughout the rarefaction range; a smaller accommodation coefficient increases G_{P}. Refs. 10 and 22 also show that the choice of kinematic model used to approximate the Boltzmann equation can cause an error of 20 % in G_{P}, where deviation is most prominent $\delta < 1$. Based on these arguments, $u(G_{\mathrm{P}})$ was evaluated by propagating four error cases through the A_0 calculation: (i) a 10 % increase in G_{P} resulted in -0.1×10^{-4} mm^2; (ii) a 0.25 increase in a_{00} resulted in $+0.5 \times 10^{-4}$ mm^2 (i.e., effect of error in the accommodation coefficient); (iii) a 0.2 increase in a_1 when $\delta < 1$ resulted in $+1.4 \times 10^{-4}$ mm^2 (i.e., effect of error approximating the Boltzmann equation); (iv) the three-part interpolation function, Eq. (11.136) in Ref. 10, for G_{P} resulted in $+0.4 \times 10^{-4}$ mm^2. The difference between Eq. (4) and each of the four G_{P} error cases is graphically shown in Figure 1(c). Therefore, the component "RGD" added to Table I is a combination of half the error between rarefied gas dynamics versus Dadson theories, plus half the range of the four error cases which cover $u(G_{\mathrm{P}})$. This is a best estimate of what contribution uncertainty in the rarefied gas dynamics model makes to $u(A_0)$, but it is based on limited information.

Despite these open questions about uncertainty in flow theory, the Sharipov model does predict the fall-rate[21]

$$v_{\mathrm{fall}} = \frac{v_{\mathrm{mp}}^2}{2\pi \mathcal{G}_{\mathrm{c}}^2 p_1} \dot{m}, \tag{9}$$

for a mass flow rate[28] $\dot{m} = -\frac{\pi(\mathcal{G}_{\mathrm{p}}+\mathcal{G}_{\mathrm{c}})}{v_{\mathrm{mp}}} G_{\mathrm{P}} h_z^2 \frac{\mathrm{d}p_z}{\mathrm{d}z}$. The generatrixes in these formulae refer to the pressure-distorted profiles. A comparison of theory with what is observed experimentally is listed in Table II, for the gas species helium, argon, and nitrogen. The estimate of uncertainty in the theoretical fall-rate is between 10 % and 14 %, and comes from half the range of v_{fall} calculated for the four error cases covering $u(G_{\mathrm{P}})$, described above. The

theoretical values have assumed $a_{00} = 0.25$ in the G_P function Eq. (4) for all gases (i.e., a tangential momentum accommodation coefficient of 0.9 for all gases interacting with polished tungsten carbide.) For experiment, $u(v_\mathrm{fall})$ is 10.8 %: measurement of cylinder position has a 10 % uncertainty in the length scale (which was calibrated with calipers), and reproducibility in the measurement is within 4 % (one standard deviation on ten measurements). Referring to Table II, the experimental v_fall agrees with theory within 8 % on average for all three gas species. For helium, it is remarkable that both experiment and theory show a reduction in v_fall as p_1 increases from 43 kPa to 93 kPa. These two facts give confidence in the validity of the flow model (and increase confidence in the FEA distortion model). Two concerns are noted: (i) Disagreement between experiment and theory appears systematic for all three species, suggestive of either the measured gap width being too wide or the theoretical G_P being too high; and (ii) A quantitative validation of the flow model requires a dedicated experiment to measure the accommodation coefficient for each species interacting with polished tungsten carbide. (Qualitative information from the literature survey of Ref. 25 suggests that the accommodation coefficient for argon would be 0.03 lower than that of helium—hence G_P larger, and theoretical v_fall faster by about 7.5 % than what is listed in Table II.)

[Additionally, the Sharipov model—Poiseuille flow with no-slip boundaries—does not presently describe the effect of rotation. A phenomenological account is due to Schmidt, Welch, and Ehrlich[29], who modeled decay in the rate of rotation as having a period $\tau = \tau_0 \exp\left(\frac{\Gamma}{I}t\right)$, where Γ is the angular torque coefficient and I is the mass moment of inertia. Schmidt, Welch, and Ehrlich used a momentum transfer function to interpolate the torque coefficient between two limiting cases, i.e., viscous and free-molecular flow regimes. The final expression for the torque coefficient, a drag caused by gas in the annular region between the piston and rotating cylinder,

$$\Gamma_\mathrm{an} = \frac{2\pi \mathcal{G}_\mathrm{c}^3}{h_z} \int_0^{l_\mathrm{c}} F_1(p_z)\mathrm{d}z, \tag{10}$$

includes the momentum transfer function $F_1 \equiv \frac{\eta}{1+\beta_1/p_z}$, with the variable $\beta_1 = \frac{2\sqrt{\pi}RT\eta}{M v_\mathrm{mp} h_z}$ chosen for smooth interpolation between the two limiting cases of flow. Experimental estimates of $\frac{\Gamma}{I}$ are obtained as the slope of a linear fit to the measured period of rotation $\ln(\tau)$ as a function of time. In the absolute mode of operation $\Gamma \approx \Gamma_\mathrm{an}$, because the contribution of drag on the rotating surfaces in the belljar is considered negligible (i.e., belljar pumped to $p_2 < 0.3$ Pa). Therefore, Eq. (10) can be compared to experimental measurements of rotation decay rates; this comparison is listed in Table III. Schmidt, Welch, and Ehrlich[29] used Eq. (10) to deduce h_z by regressing experimental data to the model; upon encountering discrepancy between h_z inferred by fall-rate versus rotational-decay, they stated preference for the latter inference. In the present case, close agreement between experiment and theory, for both fall-rate (Table II) and rotational-decay (Table III), tends to increase confidence that the artifact is understood; besides the fact that h_z is claimed known within 7.3 % (41 nm) by dimensional measurement. However, it must be pointed out that Eq. (10) is a kludge of p_z from rarefied gas dynamics[7] combined with the interpolation of limiting cases suggested by Ref. 29. The purpose of this parenthetical paragraph was to draw attention for the need of cylinder rotation to be incorporated into the rarefied gas dynamics model of the piston-gauge in a rigorous way, together with a quantitative statement as to the magnitude of vertical force on a spinning irregular shape.]

The much larger uncertainty component in the flow calculation is related to the generatrix and the imperfect geometry of the artifact. Despite the adjustments o and t to the dimensional measurements, A_0 has a variance related to variability among $\mathcal{G}$. As an example, out-of-roundness of the piston and cylinder are about 60 nm at the point of engagement. In principle, under the assumptions of viscous flow[9] (hydrodynamic regime) and axisymmetry (or, no rotation), this imperfect form can be accounted for by performing the flow calculation for each azimuthal $\mathcal{G}$ as a continuum[30]. However, continuity is not always valid in the theory of rarefied gas dynamics[22,23,31], and the assumption of axisymmetry is questionable, because out-of-roundness is six to nine times larger than uncertainty in a single diameter

TABLE III. Comparison of rotational-decay rates between experiment and theory in Eq. (10). Moments of inertia I for the rotating assembly are listed, which correspond to the mass loads generating the pressures p_1 of Table II. PCA2062 in absolute mode, $p_2 < 0.3$ Pa. The number in brackets is standard deviation on ten repeat measurements.

	$\frac{\Gamma}{I}$ /(μs^{-1})								
	He			Ar			N_2		
I /(kg m^2)	exp.	theory	% diff.	exp.	theory	% diff.	exp.	theory	% diff.
0.023	1296(168)	1217	6.4	2430(170)	2681	−9.4	2161(161)	2182	−0.9
0.171	265(16)	276	−3.9	583(11)	517	12.8	433(19)	416	4.0
0.467	156(18)	148	4.9	250(4)	238	5.3	197(4)	190	3.5
0.763	104(4)	106	−1.5	169(6)	158	7.2	133(4)	126	6.4
1.059	84(2)	83	0.0	121(8)	118	2.9	101(7)	93	7.7
1.355	70(1)	68	2.1	95(2)	93	2.1	83(5)	74	11.9

measurement. Instead, the present view accepts that imperfect geometry introduces an uncertainty component into the calculation of A_0. This component was evaluated by iterating the calculation of A_0 for all 64 permutations of piston and cylinder generatrixes (azimuthal orientations); in effect, rotating the cylinder around the piston. The standard deviation on the 64 calculations was 1.1×10^{-3} mm^2. (The range was 4.4×10^{-3} mm^2; the authoritative work of Schmidt *et al.*[16] used one-half the range as standard uncertainty. The mean of the 64 permutations of A_0 based on combinations of $\mathcal{G}$, agrees with A_0 calculated by the azimuthal average, within 1 part in 10^7; the median of the 64 permutations is 2.0×10^{-8} larger than the mean.) Again, dimensional measurements of roundness and straightness stop 2 mm short of the cylinder end, and the out-of-roundness trends 2.6 nm/mm worse towards the end: therefore, it is projected that the effect of out-of-roundness is about 10 % larger than what the 64 permutations suggest. Also, polynomial fits to the measured $\mathcal{G}$ data are used (i.e., to extrapolate $\mathcal{G}_c$, and for numerical advantage) but this "filtering" may remove actual surface feature. The standard deviation on the residuals from the fit is less than 1.5 nm, and the range is 9.5 nm: at this dimensional level, it is not clear if the polynomial fitting removes surface feature or measuring instrument noise. Nevertheless, if the "raw" measurement data is used for computation, the difference from what is obtained for the polynomial fits is only $3 \times 10^{-9} \cdot A_0$. Therefore, the entry $\mathcal{G}$ in Table I is predominantly because of imperfect cylindricity.

The width of the gap h_z varies as the cylinder falls down the piston. For the geometry of historic PG39, Jain, Bowers, and Schmidt[15] estimated that geometric effects would change the area by $1 \times 10^{-6} \cdot A_0$ as the piston moved 3.5 mm relative to the cylinder in z; Sharipov *et al.*[21] found a difference of $0.7 \times 10^{-6} \cdot A_0$ between low and high positions (i.e., relative positions of piston and cylinder that differed by 5.5 mm in z). In the present work, this effect was evaluated by iterating the calculation of A_0 as the location of the cylinder incrementally moves down the piston; in effect, sliding a window across what portion of $\mathcal{G}_p$ is used in Eq. (2) and loaded with p_z in the FEA. The result is shown in Figure 3(c); the valid "float zone" is the cylinder position range ±2.5 mm, where A_0 has a dependence of 4.0×10^{-5} mm^2/mm. The result of Figure 3(c) can be intuitively explained: A_0 reaches a maximum as the cylinder falls past the small bump in the piston profile [see Figure 2(c) at $z \approx -33$ mm], while b steadily decreases as more of the piston outer diameter is loaded with p_1. (To be clear: the piston is becoming more distorted as the cylinder falls, so the average diameter of the PCA decreases and A_{eff} decreases.) The piston-gauge has a position sensor which can monitor cylinder height within 0.2 mm. Thus, one can either record a generated pressure at a reference cylinder height corresponding to a specific calculation of A_{eff}, or compensate A_{eff} depending on the indication of cylinder height. The estimate of the h_z variation in Table I is therefore a small effect overall, for the unique geometries of PCA2062. (Measurement corroborating this calculated h_z effect follows in Section IV.)

3. Summary of $u(A_0)$

In the dimensional entries for A_0 in Table I, "extrapolation" and "compression" are treated as biases, and so add half their estimate in quadrature with the other entries. The quadrature-sum of the dimensional and flow entries results in $u(A_0)$ contributing 1.7 µPa/Pa uncertainty to a generated pressure, and is thus the dominant component. Arguments can be made that the entries $\mathcal{E}$ and $\mathcal{G}$ are duplicates, which effectively sample the same source of uncertainty—imperfect cylindricity—and therefore uncertainty is slightly overestimated. Although the origin of both entries is probably the same, they are interpreted as separate and unrelated. The entry $\mathcal{E}$ is viewed as describing the uncertainty in how well a static set of 3D dimensional measurements can be fused together and represented by a cross-sectional profile. The entry $\mathcal{G}$ is viewed as describing the uncertainty in forces arising from noncontinuous flow, as a non-axisymmetric cylinder rotates about a non-axisymmetric piston. In Section IV, indirect tests on the effect of rotation on the generated pressure suggest that the entry $\mathcal{G}$ is overestimated by factor of five for PCA2062 (or a factor of two for more typical PCA); the entry $\mathcal{G}$ is therefore precautionary, and its removal awaits a theoretical estimate for the effect of rotation on flow.

B. Minor Contributors

Knowledge of the distortion coefficient b is limited by uncertainty in elastic properties, the accuracy of the pressure distribution in the gap, and the fidelity of the finite-element model to the experiment. Salama, Sabuga, and Ulbig[32] demonstrated that the elastic properties of tungsten carbide might be measured within 0.1 % by resonant ultrasound spectroscopy; the PCA analyzed here is made from the same sintering of tungsten carbide as measured by Salama, Sabuga, and Ulbig, but Ref. 32 also showed that variations exist between batches of up to 4 %. Changing material properties by 4 % in the model resulted in a change of 1.6 % to b. From the dimensional discussion above, the gap width h_z is confidently known within 41 nm. Changing the h_z input to the model by 41 nm resulted in a change of 1.6 % to b. The aforementioned 64 permutations for piston and cylinder over all azimuthal orientations showed a standard deviation on b of 9.2 % [this uncertainty is partially accounted for by $u(\mathcal{G})$ above]. Also, Figure 3(c) shows that b can vary by as much as 6.4 % as the cylinder falls down the piston; the effect is 10 times smaller if a correction is applied for cylinder height. Finally, the pressure distribution in the gap depends on knowledge of G_P, and the quadrature-sum of the four error cases covering $u(G_\mathrm{P})$ was a 10.2 % uncertainty in b. Validation of the finite-element model is less straightforward. Neither increasing the density of the mesh, nor sample spacing on p_z, influenced b by more than 0.01 %; both the element edge size and step size in z were 0.1 mm). However, it is less certain that the boundary conditions accurately reflect the real-world. The piston is modeled as free to deform, and thus does not properly account for the friction of the clamped o-ring. The effect of this oversight should be small, because the piston distorts five times less than the cylinder. Furthermore, the PCA plumbing has a "controlled clearance port" which allows pressure applied to the internal surfaces of the piston to be independent of p_1: this feature offered an indirect validation of the FEA estimate of piston distortion, via a change in fall-rate and h_z in Eq. (9). If the inside surface of the piston remains at atmospheric pressure, the FEA predicts an increase in v_fall of 11 % at $p_1 = 500$ kPa, whereas experiment showed a 13 % increase in v_fall. This agreement suggests that o-ring friction has a small effect on piston distortion, and piston distortion makes the smaller contribution to b. For the cylinder, it is modeled as a monolithic joint between the tungsten carbide cylinder and titanium cap; in reality, the two parts are epoxied together. If a 0.1 mm layer of epoxy ($E = 1$ GPa, $\mu = 0.4$) is introduced between the cylinder and cap, b decreases by 5.2 %. (The value state above $b = 5.12(73) \times 10^{-12} \cdot \frac{p}{\mathrm{Pa}}$ is the mean of the monolithic and epoxy models.) By adding in quadrature all aforementioned variations in b, one can only claim confidence that the finite-element model can predict b within 13.9 %, with the main uncertainty owing to

$u(p_z)$—i.e., because G_P is not very well known. The statement in Table I that b contributes no more than 0.4 µPa/Pa to a generated pressure is valid for the piston-gauge operating within its specified range $p_1 - p_2 < 530$ kPa.

The mass load is predominantly made of a stack of nine 10.2 kg stainless-steel masses, one 6.4 kg stainless-steel mass, a titanium mass bell/pan, together with the cylinder of the PCA (a tungsten carbide cylinder with titanium cup); the non-stainless-steel part of the mass load, which contributes to every generated pressure, amounts to 2.1 kg. The stainless-steel masses were made of 316 alloy with magnetic susceptibility less than 0.01. The masses were calibrated in air within 35 ng/g standard uncertainty. However, because the piston-gauge operates in absolute mode, the buoyancy correction to convert the (conventional) mass calibration values to vacuum (true) mass also comes into play. The density of the masses was obtained by hydrostatic weighing a material token in fluorocarbon[33], from which (7981 ± 10) kg/m^3 was deduced. The resulting uncertainty in the stainless-steel component of the mass load is 0.1 µg/g. Lack of accurate knowledge in the density of titanium and tungsten carbide is best handled by a 8.1 mg offset term (4 % uncertainty in density). Additional offset terms[34] arise from two unstable masses: (19 ± 7) mg vacuum grease on one screw thread to prevent binding, and an elastomer o-ring subject to (0.2 ± 0.04) mg desorption of water[35]. (Šentina *et al.*[35] report a mass gain of 2 mg by water absorption into a 2.6 g o-ring; the pressure balance o-ring is 0.22 g, and of the same elastomer.) The quadrature sum of these three mass offset terms equates to the 54 mPa in Table I.

Lastly, the two remaining components in Table I. Local gravity was measured with a free-fall gravimeter, and was updated for seasonal changes. The estimate of $u(g)$ also accounts for imperfect leveling of the PCA. The vacuum gauge has an uncertainty of 0.5 % of indication, and belljar pressure, which is turbopumped, was always less than 0.5 Pa.

IV. PRETENSIONS OF LASER BAROMETRY

This closing-section describes some tests between a laser barometer and a piston-gauge. These tests say some interesting things about precision and consistency of the A_0 and b calculation described above. (For more details on laser barometry, see Section IV of Ref. 36 and references therein.)

The laser barometer was plumbed directly to the piston-gauge system. The setup for the laser barometer is similar to Ref. 37, in which a monolithic, homogeneous Fabry–Perot cavity is suspended from cables and probed with 633 nm laser. There is one crucial improvement in thermometry over Ref. 37: the laser mode between the mirrors of the cavity has been enclosed within a copper block, and the temperature of this copper block was measured with a capsule-type standard platinum resistance thermometer[38]. (The copper block does not touch the glass cavity.) This key improvement achieves the following system characteristic: for a 112 kPa charge of argon, the settling-time required for the temperature gradient between the thermometer and cavity mode to reach 0.1 mK is within 1500 s, with a time-constant of 360 s. The performance has been verified by simulation and indirect measurement. These extra details about thermal characteristics are not misplaced. The tests below demonstrate precision and reproducibility in the optical pressure at the level of ±0.1 µPa/Pa for pressures up to 500 kPa. A ±0.1 µPa/Pa precision on optical pressures is equivalent to claiming that a capsule-type standard platinum resistance thermometer, distant from the laser beam, inferred average gas temperature along the cavity mode within ±30 µK. The claim is extreme, but it is supported.

Next follows a description of three tests, in which the reproducibility and precision of the optical pressure scale is used to validate three aspects of the piston-gauge model and performance. Below, the notation $p_{\text{ops}} = \frac{2}{3A_R}(n-1)RT + \cdots$ is used to refer to the optical pressure scale, realized by measurement of argon refractivity $n-1$ at known temperature T. (The gas constant R is a fixed value; the molar polarizability A_R is a reference property of argon gas.) However, the purpose of this closing-section is cross-validation via relative differences and ratios; these tests say nothing about the accuracy of either A_{eff}^{2062} or the

properties of argon.

A. Effect of Cylinder Position

A first test used the laser barometer to monitor the small changes in the generated pressure as the cylinder fell down the piston. From Figure 3(c), the piston-gauge model predicts that the area and distortion coefficient will change. So, the first test compared a generated (calculated) pressure p_{mpg} to an optical (measured) one p_{ops} as a function of cylinder position.

The result is plotted in Figure 4(a) for operation at $p = 469$ kPa, where fractional change in pressure is shown as a function of cylinder position (fall). For the x-axis the analysis has $\delta p = p_{\mathrm{ops}} - \left(\frac{mg}{A_{\mathrm{eff}}} + p_{\mathrm{cte}} + p_{\mathrm{vac}} + p_{\mathrm{head}}\right)$. The "variable" part $p_{\mathrm{head}} = \rho g \Delta z$ of the generated pressure occurs because, relative to the laser barometer, the hydrostatic head changes as the cylinder falls down the piston. (For room-temperature argon and cylinder displacement $\Delta z = 6$ mm, $p_{\mathrm{head}} \approx 1.0$ µPa/Pa—a significant disturbance compared to the x-axis result.) The "fluctuating" part p_{vac} of the generated pressure is what is happening inside the belljar, and this was measured with a vacuum gauge. [Belljar vacuum slowly fluctuates (0.2 ± 0.1) Pa about its average, equivalent to 0.2 µPa/Pa.] The "temperature" part $p_{\mathrm{cte}} \approx -2\alpha_{\mathrm{WC}}(t_{90} - 20)p$ of the generated pressure compensates for thermal expansion of the artifact caused by changes in temperature during the fall—the resolution of this compensation is no better than 0.1 µPa/Pa. The "constant" part $\frac{mg}{A_{\mathrm{eff}}}$ of the generated pressure has $A_{\mathrm{eff}} = A_0(1+b\Delta p)$; so, it incorrectly assumes A_0 and b have no dependence on z. This assumption causes an error $\delta A_{\mathrm{eff}} = [A_0(z) - A_0(0)] + \Delta p[A_0(z)b(z) - A_0(0)b(0)]$. For the case of PCA2062, the first term $A_0(z) - A_0(0)$ fractionally increases A_{eff} by 2.5×10^{-8} as the cylinder falls from $z = 3$ mm to $z = -3$ mm, while the second term $\Delta p[A_0(z)b(z) - A_0(0)b(0)]$ dominates at $\Delta p = 469$ kPa, and fractionally decreases A_{eff} by 1.6×10^{-7}.

The net result for PCA2062 is that the "constant" part of the generated pressure is predicted to change by about 0.14 µPa/Pa for the 6 mm of cylinder displacement—a small effect. The calculated effect on p_{mpg} for the combined z-dependence of A_0 and b is shown as the dashed line in Figure 4(a). The measured error $\delta p = p_{\mathrm{ops}} - p_{\mathrm{mpg}}$ closely follows the calculation, offering good evidence that the laser barometer has corroborated this aspect of the piston-gauge model.

B. Effect of Rotation Rate

A second test used the laser barometer to monitor changes in generated pressure as the rotation rate of the cylinder naturally decelerated[29] to a stop. This test was performed in absolute mode, operating at 195 kPa with the belljar pumped to $p_{\mathrm{vac}} < 0.3$ Pa. (From Table III, at 195 kPa the time-constant for rotational-decay is about 1.1 h.)

The result is shown in Figure 4(b) for the artifact PCA2062, where the rotation rate has been discretized by the resolution of the tachometer internal to the piston-gauge system. As above, the analysis has $\delta p = p_{\mathrm{ops}} - \left(\frac{mg}{A_{\mathrm{eff}}} + p_{\mathrm{cte}} + p_{\mathrm{vac}} + p_{\mathrm{head}} + p_{\mathrm{fall}}\right)$, but with the additional "falling" part $p_{\mathrm{fall}} = -1.8 \times 10^{-8} \cdot p\Delta z$ of the generated pressure, which compensates for axial displacement of the cylinder relative to the fixed piston. Based on Figure 4(b), for any nonzero rotation, there is no evidence that the generated pressure has a dependence on rotation rate greater than 0.1 µPa/Pa. Indeed, the data support an interpretation that the generated pressure does not significantly change at zero rotation. As aforementioned, the Poiseuille flow coefficient used to calculate effective area has nonslip boundaries, which is not a complete model for the rotating cylinder. The test of Figure 4(b) suggests that the effect of rotation on flow should not change the calculated area by more than $10^{-7} \cdot A_{\mathrm{eff}}^{2062}$. Nevertheless, a theoretical estimate of this effect remains absent from the piston-gauge model.

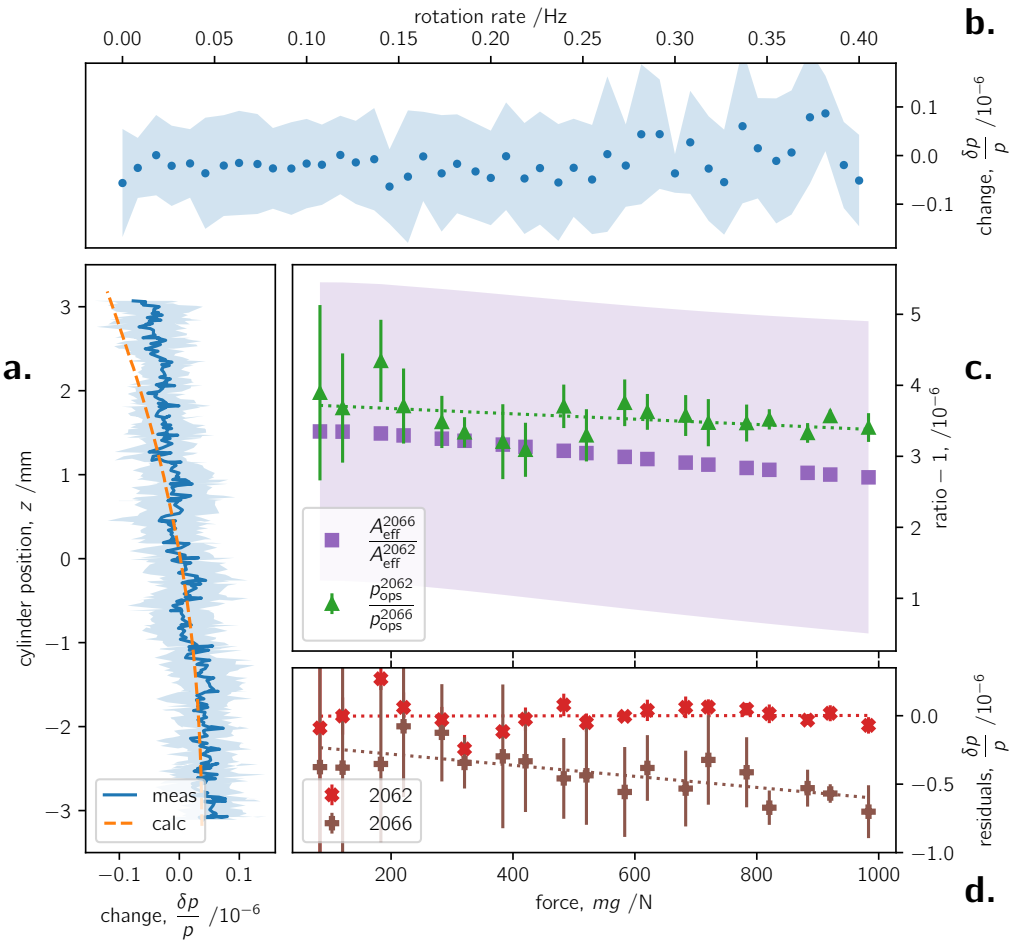

FIG. 4. Performance tests with a laser barometer. (a) Change in generated pressure as the cylinder falls down the piston. (b) Change in generated pressure as a function of cylinder rotation rate. (c) Ratios of optical pressures compared to ratios of calculated areas. (d) Residuals from Eq. (11) using coefficients $\mathcal{A}$, $\mathcal{B}$, and $\mathcal{C}$ tied to p_{mpg}^{2062}. For (a) and (b), the opaque points are the average of 10 repeats, and the shaded area spans the standard deviation. For (c) the shaded area on $A_{\text{eff}}^{2066}/A_{\text{eff}}^{2062}$ span the standard uncertainty for the calculation (see text). For (c) and (d), the errorbars on $p_{\text{ops}}^{2062}/p_{\text{ops}}^{2066}$ and δp span the standard deviation on 5 repeats.

It is mentioned that the test of Figure 4(b) was only practicable with PCA2062. The other cylinders in this set hug the piston at zero rotation, and do not float and generate pressure. Furthermore, when rotating, the other cylinders sinusoidally displace up and down the piston, with peak-to-peak amplitude of ±0.12 mm and period 330 s, independent of operating pressure. Comparisons against the laser barometer confirmed that this cylinder displacement corresponds to periodic pressure oscillations of about ±0.4 µPa/Pa, which is 20 times larger than the head effect. This noisy pressure of the other PCA will be problematic in the test below. Clearly, the test of Figure 4(b) is not the final word on the effect of rotation on the generated pressure, and should be taken as best-case. The artifact PCA2062 is considered anomalously good: it has out-of-roundness two times smaller than the other PCAs.

C. Optical Crossfloat

Finally, a third test used the laser barometer to measure optical pressure ratios between two different PCAs. With the same mass-force applied, each PCA generates a different pressure, because their areas differ. When connected to the laser barometer, each PCA "generates" two different gas refractivities, which are best converted to a respective $p_{\rm ops}$ (to account for small differences in gas temperature). To take the artifacts PCA2062 and PCA2066 as example: the ratio $p_{\rm ops}^{2062}/p_{\rm ops}^{2066}$, measured with the same mass-force applied to the respective assembly, becomes a proxy for $A_{\rm eff}^{2066}/A_{\rm eff}^{2062}$. Effectively, the approach is crossfloat by laser barometry. [The notation $p_{\rm ops}^{206x} \equiv p_{\rm ops} - (p_{\rm mass} + p_{\rm cte} + p_{\rm vac} + p_{\rm head} + p_{\rm fall})$ means the measured optical pressure has been adjusted to constant PCA conditions. This adjustment ensures that the measured quantity $p_{\rm ops}^{206x} \to F/A_{\rm eff}^{206x}$ is governed only by effective area and distortion coefficient; force F is constant. Adjustments comprise: differing cylinder masses, thermal expansion, belljar pressure, head height, and cylinder position.]

The test was performed in argon. Therefore, the area of PCA2062 stated in Section II for helium, should be updated for the different species

$$A_{\rm eff}^{2062} = 1961.0293(37)\left[1 + 6.37(73)\times 10^{-12}\frac{\Delta p}{\rm Pa}\right]\ {\rm mm}^2,$$

and the area of PCA2066 should be established in argon by the calculation methods of Section II:

$$A_{\rm eff}^{2066} = 1961.0360(55)\left[1 + 4.89(94)\times 10^{-12}\frac{\Delta p}{\rm Pa}\right]\ {\rm mm}^2.$$

So, in argon at 20 °C and absolute mode, the calculated area ratio is $A_{\rm eff}^{2066}/A_{\rm eff}^{2062} = 1.0000034(21)[1 - 1.5(13)\times 10^{-12}\frac{\Delta p}{\rm Pa}]$. From Table I, for the uncertainty of a calculated ratio, only the entries $\mathcal{E}$, flow, and b contribute; all PCA were dimensioned in the same setup[6] so that systematic error in D would be common. The stated uncertainty in the calculated ratio is dominated by the characteristics of PCA2066. Compared to PCA2062, the components $\mathcal{E}$, flow, and b for PCA2066 are larger by factors of 2.1, 2.3, and 1.4, respectively.

To deduce *absolute* optical pressures, something fundamental must be said about the properties of argon gas, and how measured refractivity at known temperature is converted to pressure[39]. These statements are deferred to a future work. Here, instead, the analysis proceeds as *relative*. The pressure generated by PCA2062 was treated as the reference, and the isothermal ($t_{90} \approx 20$ °C) refractivity measurements were fitted

$$p_{\rm mpg}^{2062} \to p_{\rm ops}^{2062} = (n-1)\mathcal{A}T\left[1 + (n-1)\mathcal{B} + (n-1)^2\mathcal{C}\right], \tag{11}$$

with $\mathcal{A} = \frac{2R}{3A_R}$. This first step tied the optical and thermophysical properties of argon gas (i.e., the proportionality coefficients $\mathcal{A}$, $\mathcal{B}$, and $\mathcal{C}$) to the diameter of PCA2062, so that $p_{\rm ops}^{2062} \equiv p_{\rm mpg}^{2062}$ in the least-squares sense. Then, without further adjustment to the proportionality coefficients, the refractivity and temperature data from the PCA2066 isotherm were processed with the right-hand side of Eq. (11) to obtain $p_{\rm ops}^{2066}$. This ratiometric/relative analysis produces the desired $p_{\rm ops}^{2062}/p_{\rm ops}^{2066}$, and it also offers some insight into nonlinearity as explained below. [The measurements reported here are so precise that the temperature dependence of $\mathcal{B}$ and $\mathcal{C}$ in Eq. (11) should be included, even for the few millikelvin fluctuation on the isotherm. Details on these dependencies are also deferred to a future work.]

The ratios $A_{\rm eff}^{2066}/A_{\rm eff}^{2062}$ and $p_{\rm ops}^{2062}/p_{\rm ops}^{2066}$ are plotted in Figure 4(c), which shows excellent agreement. The average difference is 0.5 µPa/Pa. At zero force, area ratios are independent of the distortion coefficient b, and the difference is within 0.3 µPa/Pa. The result of Figure 4(c) greatly increases confidence in the piston-gauge model and area calculation: it is independent confirmation that ratios of calculated areas are equivalent to ratios of measured pressures within 0.3 µPa/Pa. Some experimental details are mentioned. In these

crossfloat tests, each of the 19 set pressures were repeated 5 times. A repeat measurement entailed a pumpout to high-vacuum and a refill with pure argon (and refloat of the PCA). A fully-automated 95-point isotherm took 85 h to acquire. The switch between PCA2062 and PCA2066 broke the pure gas volume, but an overnight pumpout removed all contaminants before the second isotherm was acquired.

An alternate analysis of the optical crossfloat obviates the adjustment to F/A_{eff}^{206x}, but its interpretation is less clear. The alternate analysis adds an offset to Eq. (11), and $\mathcal{A}$, $\mathcal{B}$, and $\mathcal{C}$ are free parameters when *both* PCA datasets are regressed. A pressure offset term in Eq. (11) is justified, such as might arise from mass error in the piston-gauge, or glass temperature error (cavity expansivity) in the laser barometer. The analysis seeks the ratio $(\mathcal{A}^{2062}/\mathcal{A}^{2066})_T$ as proxy for $A_{\text{eff}}^{2066}/A_{\text{eff}}^{2062}$, and the optical measurements (fit coefficients) are adjusted to isothermal argon (constant and same temperature in both runs). Effectively, the analysis uses single-isotherm refractive-index gas thermometry[5] as the consistency check on pressures generated with two different PCA. The disagreement between isothermal $(\mathcal{A}^{2062}/\mathcal{A}^{2066})_T$ and the calculated area ratio $A_{\text{eff}}^{2066}/A_{\text{eff}}^{2062}$ was within 0.7×10^{-6}. While this analysis bounds combined inconsistency in A_0 and b, a full understanding is veiled by fitting effects in gas thermometry. For example, the nonlinear terms in Eq. (11) would be best identified by multi-isotherm regression, and an argument can be made that the ratio $(\mathcal{A}^{2062}/\mathcal{A}^{2066})_T$ should be produced with fixed $\mathcal{B}$ and $\mathcal{C}$ (i.e., it is the same gas at the same temperature). If the analysis is performed with $\mathcal{B}$ and $\mathcal{C}$ being the (fixed) average value of both PCA datasets, and leaving $\mathcal{A}$ and the offset as free parameters, disagreement between the measured (fit) and calculated ratios reduces to 0.2×10^{-6}. Further discussion about fitting effects in gas thermometry is outside the scope of the present article, and these sub-$10^{-6} \cdot p$ difficulties comparing mechanical and optical ratios are set aside. Next, some useful information is obtained by looking at the residuals.

The residuals plotted in Figure 4(d) have $\delta p = p_{\text{ops}} - p_{\text{mpg}}$. From above, $p_{\text{ops}}^{2062} \equiv p_{\text{mpg}}^{2062}$ in the least-squares sense, so a linear fit to δp^{2062} has a mean and slope approximately zero. However, three pieces of quasi-independent information can be unraveled from the residuals:

1. The nonzero mean of δp^{2066} is synonymous with $A_{\text{eff}}^{2066}/A_{\text{eff}}^{2062} - p_{\text{ops}}^{2062}/p_{\text{ops}}^{2066} \neq 0$ from Figure 4(c) and above; y-axis intercept has $\delta p^{2066} = -0.2$ µPa/Pa. This nonzero intercept is caused by the combined effect of error in the dimensioning, error in the piston-gauge model, plus irreproducibility of the laser barometer (refractometer plus thermometer). It is difficult to conceive irreproducibility in the (untouched) laser barometer exceeding 0.2 µPa/Pa across the eight-day duration of the two optical crossfloats. Consequently, δp^{2066} is interpreted as confirmation that the piston-gauge model (i.e., the conversion of diameter to generated pressure) is consistent within 0.4 µPa/Pa, and that the dimensional characterization is consistent within 10 nm. (To be clear, this does not mean diameters are known within 10 nm; rather, statistical error in the dimensional characterization is less than 10 nm.)

2. The nonzero slope on δp^{2066} is caused by the combined effect of error in the piston-gauge flow model plus error in the calculation of the distortion coefficient. As above, it is difficult to conceive compressibility of the laser barometer changing during the eight-day (isothermal) test; this assumption is largely confirmed by the δp^{2062} residuals. The 4.1×10^{-10} /N slope on δp^{2066} means that the error in the distortion coefficient b calculated for a single PCA might be as large as $\frac{1}{\sqrt{2}} 8.8 \times 10^{-13}$ /Pa, or 12.4 %. The result is somewhat surprising. On the one hand, it is within the allowable 24 % mutual standard uncertainty of b for PCA2062 and PCA2066; on the other hand, this failure to accurately predict b is of significance to gauges operating $p > 1$ MPa. [To be clear, the slope on δp^{2066} does not mean all distortion error is in the calculation of b^{2066}; the more correct interpretation is that error in the calculation of b^{2062} has been written onto the properties of argon gas in the initialization of Eq. (11).]

3. Little about both sets of residuals δp^{2062} and δp^{2066} suggests nonlinearity. The larger residuals δp^{2066} can be attributed to the ±0.4 µPa/Pa oscillating pressure of PCA2066

as it rotates; the magnitude of these residuals conforms with the entry $\mathcal{G}$ in Table I. For δp^{2062}, standard deviation on the residuals is less than 0.2 µPa/Pa—a remarkable result. Even if the hint of nonlinearity in Figure 4(d) were real, it is unclear to which instrument the nonlinearity should be attributed. [An imprint of nonlinearity might appear from statistically imperfect application of Eq. (11), for example.] For the refractometer, it is difficult to imagine nonlinearity in a monolithic, homogeneous block of glass suspended by cables. At these low-pressures, nonlinearity in elastic properties[40] is negligible. Similarly, at these gas densities, the higher-order terms truncated from Eq. (11) are below 0.1 µPa/Pa. Also, Ref. 41 presented good evidence that two intercompared refractometers are linear within 0.1 µPa/Pa for pressures up to 180 kPa. These three considerations vouch that nonlinearity in δp should not be attributed to p_{ops}. However, the refractometer is not absolved because this single-cavity configuration has offset errors of about 30 mPa, which would explain some of the low-pressure structure. Moreover, unexpected behavior has been observed in a similar homogeneous refractometer by Yang, Rubin, and Sun[42], some 150 times larger than the structure in Figure 4(d) (see their Figure 14). For the piston-gauge, rarefied gas dynamics and the calculation methods of Section II predict no nonlinearity greater than ±0.04 µPa/Pa; see Figure 3(b). However, the piston is clamped in an inhomogeneous assembly, and the cylinder is monolithically inhomogeneous—it is made with an epoxy-joint between the tungsten-carbide cylinder and titanium cup. In principle, these inhomogeneities may give rise to nonlinearity as a function of pressure that would be lost by an idealized model; however, it would instinctively seem that the very high elastic modulus of tungsten-carbide should ensure the distortion coefficient b is immune to mismatch effects. So, the present work makes no firm conclusion about nonlinearity in a piston-gauge or a laser barometer; however, Figure 4(d) attests that any nonlinearity would be very small.

D. Summary of the Laser Barometer Tests

The tests reported in this closing-section have validated several aspects of the area calculation outlined in Section II. The success of these tests adds confidence that the piston-gauge model is a reliable physical description of the artifact standard, within the uncertainty stated in Table I. The findings of the tests are:

- The pressure generated by the piston-gauge changes as the piston falls down the cylinder. Optical measurements agree with calculation within 0.1 µPa/Pa.

- An experimental estimate has been placed on how much error may arise by the fact that rotation is not accounted for in the flow model. Tests that monitored the generated pressure as the cylinder decelerated to a stop suggest that this error is no larger than 0.1 µPa/Pa in PCA2062, an artifact of unusually good form. This experimental estimate lacks theoretical confirmation.

- An optical crossfloat produced a ratio of two measured pressures, generated by two respective PCA. The ratio of measured pressures agreed with the ratio of calculated areas within 0.3 µPa/Pa. Additionally, when generated pressures from the two PCA are compared to the optical pressure scale, the trend (slope) in disagreement confirms that error in the calculated distortion coefficient b is no larger than 12.4 %.

- Any hint of nonlinearity in either the piston-gauge or laser barometer is no larger than 0.2 µPa/Pa for PCA2062. The present tests have not identified the more nonlinear instrument. It must be stated that, if real and attributable to the piston-gauge, nonlinearity would be an order of magnitude smaller than the combined uncertainty stated in Table I.

V. CONCLUSION

A procedure has been described to convert a dimensional dataset to effective area for a piston–cylinder assembly. The procedure first fuses together all dimensional inputs (diameter, straightness, and roundness) to form the birdcage and average generatrix. The flow (distributed pressure) down the gap between piston and cylinder is then calculated using the theory of rarefied gas dynamics. Next, the distributed pressure is parameterized to load a finite-element model, which estimates geometric distortion to the generatrixes. Finally, the calculation is iterated to convergence. The entire procedure runs in a self-contained script, which executes the finite-element program as a function call.

Based on the quality of the dimensional characterization, its reproducibility, and a detailed error analysis, it seems realistic that the artifact PCA2062 can approach 2 µPa/Pa standard uncertainty. From an optimistic viewpoint, this work has reported some ratio and relative tests against a laser barometer which suggest that the reproducibility, precision, and linearity of the artifact standard are an order of magnitude smaller than this uncertainty estimate. The counterpoint recalls the authoritative work of Schmidt *et al.*[16] claimed $3.0 \times 10^{-6} \cdot p$ uncertainty on the 36 mm diameter PCA39. When scaled for differences in diameter, the work of Schmidt *et al.* translates to $2.2 \times 10^{-6} \cdot p$ for the 50 mm diameter PCA2062. The pessimistic view holds that despite a generation of progress in dimensional metrology and flow modeling, the performance of the (other) last artifact-based standard[2] remains essentially unchanged. Indeed, if anything, recent evidence in key comparisons of diameter[43,44], urge caution below the 4 µPa/Pa level (100 nm in diameter). Crossfloat comparisons that show agreement between force and diameter ratios at fractionally within 10^{-6} may lead to false-confidence: ratios validate consistency of the dimensional characterization, not its accuracy. A stringent test is desired between the optical and mechanical pressure scales at the level of a few $10^{-6} \cdot p$.

ACKNOWLEDGMENTS

This work was greatly assisted by Fluke Calibration, who hosted one of the authors (PFE) for a workshop in Phoenix AZ in April 2019. Robert Haines and Michael Bair at Fluke Calibration provided essential guidance in the operation of a state-of-the-art piston-gauge.

Initial work on the area/flow of PCA2062 was undertaken in the second-half of 2015 by Felix Sharipov from the Universidade Federal do Paraná, Curitiba, and Yuanchao Yang from the National Institute of Metrology, Beijing. Their working-report "Effective cross section of piston–cylinder gauges," dated January 27, 2016, was the starting-point for Section II in this article.

Appendix A: Supplementary information

The supplementary material to this article is available at https://doi.org/10.18434/mds2-2698. The supplementary material is an archive file, containing the dimensional dataset of PCA2062 and the conversion scripts.

- The main Python script is `CalcAeff2062.py`. This script controls the area conversion process, and runs standalone. It has two dependencies. First, it calls `findGcyl2062.py` and `findGpis2062.py`. These two scripts load the dimensional datasets and find the best-fit generatrixes of piston and cylinder. The second dependency is that a finite-element program is required to calculate distortion. The present implementation uses Ansys[45]. The main script `CalcAeff2062.py` dynamically updates the finite-element scripts for the applied pressure load distributed down the gap, and runs Ansys as a function call.

- The dimensional datasets of the piston–cylinder assembly PCA2062 are included. The dimensional characterization was undertaken in Fall 2020. The dataset comprises straightness and roundness traces, and two-point diameters.

[1] K. Jousten, "A unit for nothing," Nature Physics **15**, 618 (2019).
[2] W. D. Phillips, "The end of artefacts," Nature Physics **15**, 518 (2019).
[3] G. F. Molinar, B. Rebaglia, A. Sacconi, J. C. Legras, G. P. Vailleau, J. W. Schmidt, J. R. Stoup, D. R. Flack, W. Sabuga, and O. Jusko, "CCM key comparison in the pressure range 0.05 MPa to 1 MPa (gas medium, gauge mode). Phase A1: Dimensional measurements and calculation of effective area," Metrologia **36**, 657–662 (1999).
[4] M. Perkin, R. Köhler, P. Riety, T. Skrovanek, E. C. Morris, C. R. Tilford, C. D. Ehrlich, A. Ooiwa, G. Eichorn, J. Jäger, G. F. Molinar, A. H. Bass, and A. C. Gupta, "Comparison of pressure standards in the range 10 kPa to 140 kPa," Metrologia **35**, 161–173 (1998).
[5] P. M. C. Rourke, "Perspective on the refractive-index gas metrology data landscape," Journal of Physical and Chemical Reference Data **50**, 033104 (2021).
[6] J. Stoup, W. Ren, E. Stanfield, and P. Egan, "Piston-sleeve diameter characterization at NIST," In preparation for Metrologia.
[7] W. Sabuga, F. Sharipov, and T. Priruenrom, "Determination of the effective area of piston–cylinder assemblies using a rarefied gas flow model," in *PTB-Mitteilungen*, Proceedings of the 5th CCM International Conference on Pressure and Vacuum Metrology, Vol. 121, edited by K. Jousten (Physikalisch-Technische Bundesanstalt, 2011) pp. 260–262.
[8] W. Sabuga and T. Priruenrom, "An approach to the evaluation of dimensional measurements on pressure-measuring piston-cylinder assemblies," in *Proceedings of the Joint International Conference IMEKO TC3/TC16/TC22* (2007).
[9] R. S. Dadson, S. L. Lewis, and G. N. Peggs, *The pressure balance: theory and practice* (Her Majesty's Stationery Office, London, 1982).
[10] F. Sharipov, *Rarefied Gas Dynamics: Fundamentals for Research and Practice* (Wiley-VCH, Weinheim, Germany, 2016) Chap. 11 & App. B.
[11] R. S. Dadson, R. G. P. Greig, and A. Horner, "Developments in the accurate measurement of high pressures," Metrologia **1**, 55–67 (1965).
[12] A. H. Bass, "Analysis of mechanical pressure generators," Journal of Physics E: Scientific Instruments **11**, 682–688 (1978).
[13] F. Sharipov, "Application of the Cercignani–Lampis scattering kernel to calculations of rarefied gas flows. I. plane flow between two parallel plates," European Journal of Mechanics B/Fluids **21**, 113–123 (2002).
[14] S. S. Lo, S. K. Loyalka, and T. S. Storvick, "Rarefied gas flow in a cylindrical annulus," Journal of Vacuum Science & Technology A **1**, 1539–1548 (1983).
[15] K. Jain, W. Bowers, and J. W. Schmidt, "A primary dead-weight tester for pressures (0.05–1.0) MPa," Journal of Research of the National Institute of Standards and Technology **108**, 135–145 (2003).
[16] J. W. Schmidt, K. Jain, A. P. Miiller, W. J. Bowers, and D. A. Olson, "Primary pressure standards based on dimensionally characterized piston/cylinder assemblies," Metrologia **43**, 53–59 (2006).
[17] E. Stanfield, J. Stoup, M. Braine, and T. Doiron, "Sphere diameter interferometry with nanometer uncertainty," Metrologia **57**, 025003 (2020).
[18] J. Stoup and T. Doiron, "A novel high accuracy micrometer for the measurement of diameter," Metrologia **58**, 025002 (2021).
[19] C. M. Sutton and M. P. Fitzgerald, "Performance aspects of gas-operated pressure balances as pressure standards," Metrologia **46**, 655–660 (2009).
[20] W. Sabuga, "Pressure measurements in gas media up to 7.5 MPa for the Boltzmann constant redetermination," in *PTB-Mitteilungen*, Proceedings of the 5th CCM International Conference on Pressure and Vacuum Metrology, Vol. 121, edited by K. Jousten (Physikalisch-Technische Bundesanstalt, 2011) pp. 247–255.
[21] F. Sharipov, Y. Yang, J. E. Ricker, and J. H. Hendricks, "Primary pressure standard based on piston-cylinder assemblies. Calculation of effective cross sectional area based on rarefied gas dynamics," Metrologia **53**, 1177–1184 (2016).
[22] F. Sharipov and V. Seleznev, "Data on internal rarefied gas flows," Journal of Physical and Chemical Reference Data **27**, 657–706 (1998).
[23] S. A. Schaaf, "Modern developments in gas dynamics," in *Modern Developments in Gas Dynamics*, edited by W. H. T. Loh (Springer US, Boston, MA, 1969) Chap. 6. Rarefied Gas Dynamics, pp. 235–254.
[24] F. Sharipov, "Data on the velocity slip and temperature jump on a gas-solid interface," Journal of Physical and Chemical Reference Data **40**, 023101 (2011).
[25] A. Agrawal and S. V. Prabhu, "Survey on measurement of tangential momentum accommodation coefficient," Journal of Vacuum Science & Technology A **26**, 634–645 (2008).
[26] F. Sharipov and M. R. Moldover, "Energy accommodation coefficient extracted from acoustic resonator experiments," Journal of Vacuum Science & Technology A **34**, 061604 (2016).
[27] M. L. Huber, E. W. Lemmon, I. H. Bell, and M. O. McLinden, "The NIST REFPROP database for highly accurate properties of industrially important fluids," Industrial & Engineering Chemistry Research **61**, 15449–15472 (2022).

[28]F. M. Sharipov and V. D. Seleznev, "Rarefied gas flow through a long tube at any pressure ratio," Journal of Vacuum Science & Technology A **12**, 2933–2935 (1994).
[29]J. W. Schmidt, B. E. Welch, and C. D. Ehrlich, "Operational mode and gas species effects on rotational drag in pneumatic dead weight pressure gauges," Measurement Science and Technology **4**, 26–34 (1993).
[30]M. Caubergh, J. Draïsma, G.-J. Franx, G. Hek, G. Prokert, S. Rienstra, and A. Verhoeven, "Measure under pressure: Calibration of pressure measurement," in *55th European Study Group: Mathematics with Industry* (2007).
[31]W. Marques Jr., G. M. Kremer, and F. M. Sharipov, "Couette flow with slip and jump boundary conditions," Continuum Mechanics and Thermodynamics **12**, 379–386 (2000).
[32]A. D. Salama, W. Sabuga, and P. Ulbig, "Measurement of the elastic constants of pressure balance materials using resonance ultrasound spectroscopy," Measurement **45**, 2472–2475 (2012).
[33]Z. J. Jabbour and S. L. Yaniv, "The kilogram and measurements of mass and force," Journal of Research of the National Institute of Standards and Technology **106**, 25–46 (2001).
[34]M. Bair, "A new primary standard for the realization of pressure from 10 to 500 kPa," in *Simposio de Metrología*, edited by C. A. Galván-Hernández (CENAM, Santiago de Querétaro, Mexico, 2010) pp. 1–9.
[35]J. Šetina, M. Sefa, B. Erjavec, and D. Hudoklin, "Measurement and modeling of water-vapor diffusion in elastomers with impact in humidity and vacuum measurements," International Journal of Thermophysics **34**, 412–423 (2013).
[36]J. Scherschligt, J. A. Fedchak, Z. Ahmed, D. S. Barker, K. Douglass, S. Eckel, E. Hanson, J. Hendricks, N. Klimov, T. Purdy, J. Ricker, R. Singh, and J. Stone, "Review article: Quantum-based vacuum metrology at the National Institute of Standards and Technology," Journal of Vacuum Science & Technology A **36**, 040801 (2018).
[37]P. F. Egan, "Capability of commercial trackers as compensators for the absolute refractive index of air," Precision Engineering **77**, 46–64 (2022).
[38]P. Egan, "Rapid response optical RIGT, and relative determination of $T - T_{90}$ across ($293 < T < 433$) K," in *AIP Conference Proceedings*, Temperature: Its measurement and control in science and industry, volume 9, edited by C. Meyer (AIP, 2024).
[39]P. F. Egan, J. A. Stone, J. K. Scherschligt, and A. H. Harvey, "Measured relationship between thermodynamic pressure and refractivity for six candidate gases in laser barometry," Journal of Vacuum Science & Technology A **37**, 031603 (2019).
[40]K. Kondo, S. Iio, and A. Sawaoka, "Nonlinear pressure dependence of the elastic moduli of fused quartz up to 3 GPa," Journal of Applied Physics **52**, 2826–2831 (1981).
[41]P. F. Egan, J. A. Stone, J. E. Ricker, and J. H. Hendricks, "Comparison measurements of low-pressure between a laser refractometer and ultrasonic manometer," Review of Scientific Instruments **87**, 053113 (2016).
[42]Y. Yang, T. Rubin, and J. Sun, "Characterization of a vacuum pressure standard based on optical refractometry using nitrogen developed at NIM," Vacuum **194**, 110598 (2021).
[43]G. B. Picotto, "Final report on EUROMET.L-K4: Calibration of diameter standards, group 1," Metrologia **47**, 04003 (2010).
[44]E. Bánréti, "Final report on EUROMET.L-K4: Calibration of diameter standards, group 2," Metrologia **47**, 04001 (2010).
[45]Certain equipment, instruments, software, or materials, commercial or non-commercial, are identified in this paper in order to specify the experimental procedure adequately. Such identification is not intended to imply recommendation or endorsement of any product or service by NIST, nor is it intended to imply that the materials or equipment identified are necessarily the best available for the purpose.